

1 Gas self-diffusion in different local environments of mixed-
2 matrix membranes as a function of UiO-66-NH₂ metal–organic
3 framework loading

4
5 Omar Boloki¹, Stephen Dewitt², Eric T. Hahnert², Zachary Smith², Sergey Vasenkov^{1*}

6
7 ¹ Department of Chemical Engineering, University of Florida, Gainesville FL 32611, USA

8 ² Department of Chemical Engineering, Massachusetts Institute of Technology, Cambridge,
9 Massachusetts 02139, USA

10
11
12
13
14
15
16
17 *Corresponding Author. Tel.: +1 352 392 0315; *Email address*: svasenkov@che.ufl.edu (S.
18 Vasenkov).

19 **Abstract**

20

21 This work focuses on quantification of microscopic self-diffusion of gas molecules in mixed-
22 matrix membranes (MMMs) formed by dispersing UiO-66-NH₂ metal-organic framework (MOF)
23 particles in a 6FDA-Durene polyimide. Self-diffusion measurements were performed by ¹³C
24 pulsed field gradient nuclear magnetic resonance (PFG NMR) for pure CO₂ and CH₄ with spatial
25 resolutions in the range of 0.5 – 24 microns and for different MOF loadings between 12.5 and 50
26 weight percent. Diffusion measurements for the MMM with the lowest MOF loading of 12.5
27 weight percent yielded a single diffusivity for each gas for all measured times corresponding to
28 diffusion under the condition of a fast exchange between the UiO-66-NH₂ crystals and the
29 surrounding polymer phase. However, as the UiO-66-NH₂ loading was increased, two molecular
30 ensembles were observed for both CO₂ and CH₄: 1) an ensemble corresponding to diffusion inside
31 UiO-66-NH₂ crystals and through the MOF-polymer interfaces, and 2) an ensemble corresponding
32 to diffusion mainly in the polymer phase of the MMMs. This behavior can be explained by the
33 formation of MOF clusters at higher MOF loadings. Quantification of the intra-cluster diffusivity,
34 average cluster size, and the dependence of these properties on the MOF loading are presented and
35 discussed. The reported measurements can serve as a framework to quantify discrete microscopic
36 diffusion characteristics and sizes of interconnected MOF clusters in MMMs as MOF loading
37 increases to reach the desired outcome of gas percolation over a spanning MOF cluster, viz a
38 cluster of interconnected MOF crystals spanning an entire MMM.

39

40 **Keywords:** Diffusion, PFG NMR, Mixed-matrix membranes, UiO-66-NH₂, Gas separations

41 1. Introduction

42 Membrane-based gas separations [1-4] is a growing industrial technology that offers a
43 potential alternative to legacy gas separation processes, including unit operations like amine-based
44 absorption to capture CO₂ from various feed streams and cryogenic distillation for molecular
45 fractionation [3, 5]. Membrane technology can provide advantages such as improved energy
46 efficiency, simple operation, potential cost savings, and a lower environmental impact in
47 comparison to incumbent separation technologies [2, 3, 5]. However, all large-scale commercial
48 gas separation membranes are made from polymers, and these materials are subject to an intrinsic
49 tradeoff between permeability and selectivity [3, 4] known as the Robeson upper bound [6, 7]. One
50 approach to overcome these intrinsic tradeoffs is through the development of mixed-matrix
51 membranes (MMMs), which can surpass polymer performance limits by incorporation of solid
52 porous fillers [8-11]. MMMs combine separation performance advantages offered by the filler
53 with the mechanical and scale-up properties of polymeric materials [3, 5, 9, 12]. MMMs have been
54 explored for applications in gas separations, heavy metal removal, water purification, and
55 microfiltration, among others [13, 14]. There are various types of fillers that can be used in MMMs,
56 including zeolites, carbon molecular sieves (CMS), and metal-organic frameworks (MOFs).
57 Recently, there has been a growing interest in research focusing on MMMs formed with MOF
58 fillers. MOFs are composed of metals or metal-oxo clusters that are bridged by organic ligands [3,
59 11, 13]. MOFs exhibit great potential in gas separations due to their high chemical and thermal
60 stability, as well as their ultra-high, uniform, and tunable porosity [3, 14, 15].

61 In recent years, the UiO-66 MOF [16, 17], which contains zirconium-oxo clusters of
62 Zr₆O₄(OH)₄ as metal nodes that are bridged by terephthalic acid (BDC) ligands, has attracted
63 significant interest [15-17]. Beyond the native framework, the BDC ligands can be functionalized

64 with a variety of derivatives, producing a range of functional UiO-66 MOFs, such as UiO-66-NH₂
65 and UiO-66-NO₂ [5, 17-19]. Among these structural analogs, the primary amine-functional MOF
66 is of particular interest. Cmarik *et al.* studied the adsorption properties of four different derivatives
67 of UiO-66 [19] and revealed that UiO-66-NH₂ showed the highest uptake of CO₂, CH₄, and N₂ at
68 298 K. Thus, this functional MOF is of great interest for a variety of gas separation applications.

69 Quantifying transport properties of MMMs as a function of MOF loading is required to
70 evaluate and optimize separation performance. However, as composite materials, MMMs have
71 disparate local environments, including regions of the polymer, filler, and corresponding
72 interfaces. Typically, the effective macroscopic gas diffusion throughout the entire MMM is
73 quantified through permeation, uptake, and related measurements [5, 9, 18]. Effective medium
74 approaches (EMAs) are commonly used models to infer properties of each phase from the
75 macroscopic measurements. Among these models, the Maxwell and Bruggeman models are most
76 widely applied for MOF-based MMMs [20]. Unfortunately, these models infer permeabilities in
77 the MOF phase based on macroscopic permeability measurements of the pure polymer and
78 variable-loading MMMs. More direct metrologies are needed to evaluate transport properties in
79 each phase directly. Without these direct measurements, common model assumptions, such as the
80 absence of polymer rigidification and the absence of polymer–MOF interfacial defect, cannot be
81 verified, but only inferred [4]. Thus, to provide more direct and fundamental insights to transport
82 in composite systems, especially insights related to interfacial phenomena, characterization of
83 microscopic gas diffusion at relevant and localized length scales is needed. These data are
84 exceedingly rare in the literature, leaving a key knowledge gap that is needed to support widely
85 available macroscopic permeability, diffusion, and sorption data.

86 Pulsed field gradient nuclear magnetic resonance (PFG NMR) has been proven to be a
87 technique of choice to quantify microscopic self-diffusion of light gases (i.e., CO₂, CH₄, C₂H₄,
88 C₂H₆) in MMMs[10, 12, 21]. Previous PFG NMR studies were performed with MMMs where
89 fillers were crystals of zeolitic imidazolate frameworks (ZIFs), a subclass of MOFs. In this work,
90 ¹³C PFG NMR was applied to study microscopic self-diffusion of two industrial gases (CH₄ and
91 CO₂) in MMMs containing UiO-66-NH₂ crystals with sizes of around 0.76 μm, which approach
92 those typically used in MMMs. In contrast to the previous PFG NMR studies of MMMs, the
93 current work focuses on quantifying and understanding the dependence of intra-MMM
94 microscopic diffusion as a function of increasing MOF loading in the MMM. The measurements
95 were performed at high magnetic field of 17.6 or 14 T and at large magnetic field gradient
96 amplitudes up to 23 T/m. The latter allowed performing PFG NMR measurements for
97 displacements of gas molecules as small as 0.5 μm. These measurements were then analyzed to
98 determine different diffusion rates within the composite material for each gas over a range of
99 temperatures and loading pressures. These results allow for the differentiation between diffusion
100 within the MOF phase and within the polymer region.

101 **2. Experimental**

102 **2.1 Materials for Mixed Matrix Membrane Fabrication**

103 Self-diffusion of CO₂ and CH₄ was studied in a dense film of 6FDA-Durene polyimide and
104 MMMs composed of UiO-66-NH₂ with the following MOF loadings i) 12.5 wt% ii) 25 wt% and
105 iii) 50 wt%. 6FDA-Durene was purchased from Akron Polymer Systems and used without further
106 purification. UiO-66-NH₂ was synthesized by combining 410.0 mg of ZrCl₄ with 319.0 mg of 2-
107 aminoterephthalic acid, 59.02 mL of glacial acetic acid (600 eq.), 100 μL of distilled water, and
108 140.9 mL of anhydrous dimethyl formamide (DMF). The reaction mixture was heated for 24 hours

109 at 393 K and then sonicated and centrifuged to collect the precipitated product. The product was
110 subsequently washed twice with DMF, twice with methanol, and once with chloroform before
111 suspension and storage in a chloroform solution.

112 **2.2 Mixed Matrix Membrane Fabrication**

113 UiO-66-NH₂ nanoparticles suspended in chloroform were analyzed via TGA to determine the
114 wt% of nanoparticles in suspension. An aliquot of this suspension was then separated and
115 concentrated or diluted to reach a suspension of particles in 7.6 mL of chloroform. 6FDA-Durene
116 was then added to the suspension such that the total weight of 6FDA-Durene and UiO-66-NH₂
117 totaled 380 mg resulting in a casting solution of less than 5 wt%. This suspension was then left to
118 mix on a roller table for 8 hours before being cast with a filtered syringe into a glass petri dish and
119 covered by a glass plate. The suspension was then left to evaporate in a hood until a solid film was
120 formed. This film was placed in a vacuum oven at 353 K for 12 hours to remove any remaining
121 solvent from the film.

122 **2.3 Characterization**

123 The structure of the UiO-66-NH₂ nanoparticles was analyzed using a FEI Tecnai multipurpose
124 transmission electron microscope (TEM). The nanoparticles were observed by diluting two drops
125 of a suspension of UiO-66-NH₂ in 10 mL methanol and applying the suspension to a PELCO
126 100mesh copper grid acquired from Ted Pella. Images obtained from these micrographs were then
127 analyzed using Image J software to determine particle size distributions (Figure S1). The
128 crystallinity of the MOF particles in powder form was analyzed using a Rigaku Smartlab
129 multipurpose x-ray diffractometer (XRD) in the 2θ region from 5 to 50° (Figure S2). The cross-
130 sectional morphologies of all MMM films were observed using a Zeiss Merlin high-resolution

131 scanning electron microscope (SEM) after the films were fractured under liquid nitrogen (Figure
132 S3).

133 **2.4 Preparation of NMR samples**

134 To prepare PFG NMR samples, films were cut into strips of 2 – 3 mm in width and 5 – 10 mm
135 in height. To prepare each sample, around 100 mg of strips were packed in a 5 mm medium walled
136 NMR tube (Wilmad Labglass, Inc). The NMR tube was then connected to a custom-made vacuum
137 system, where the sample was degassed at 373 K for 8 hours under high vacuum to ensure that the
138 films were sorbate free before testing. After activation, the sample remained under vacuum and
139 cooled to ambient temperature (298 K). Single component gases (CH_4 or CO_2) were loaded into
140 the sample through cryogenic condensation with the desired amount of gas using liquid nitrogen.
141 Following sorbate loading, the NMR tube was flame sealed and disconnected from the vacuum
142 system. To ensure sorption equilibrium at an ambient temperature of 298 K, NMR tubes were left
143 at this temperature for at least 8 hours after loading before performing any experiments. The
144 sorbates selected for the study were ^{13}C enriched CO_2 and CH_4 . Both sorbates were of 99 %
145 isotopic purity (Sigma Aldrich).

146 Before any NMR measurements, each sample was kept for at least 1 hour in the NMR
147 spectrometer at the desired measurement temperature (either 253 or 308 K) to ensure sorption
148 equilibrium. To confirm the time selected (1 hour) was sufficient to reach the sorption equilibrium
149 selected experiments were repeated after several hours to check the reproducibility of the results.
150 It was confirmed that the results remained unchanged, within uncertainty, including no change in
151 the sorbate intra-membrane concentrations, which were determined as discussed below.

152 Sorbate loadings were estimated using NMR spectroscopy (Tables S1 – S6) taking advantage
153 of the proportionality of the area under the NMR spectrum and the number of the corresponding
154 sorbate molecules in the sample, as is in our previous studies [10, 21-23]. NMR measurements of
155 reference samples containing only bulk gases at a known pressure with no MMM added were
156 performed to obtain the proportionality constants between the amount of sorbate and the area under
157 the NMR spectrum. The total NMR signal measured in the MMM samples contained contributions
158 from molecules located in the intra-membrane region and the surrounding bulk gas phase of the
159 sample. These relative contributions were quantified using a mass balance with the following
160 known properties: (i) volume of the sealed NMR tube, (ii) total mass of the gas in the NMR tube,
161 (iii) the total volume and mass of the film samples and the volume of the surrounding gas phase in
162 the active range of the NMR radiofrequency coil. The intra-membrane gas concentrations
163 calculated using this approach are presented in Tables S3-S6. These concentrations can also be
164 quantified based on the ^{13}C T_2 NMR measurements [24, 25] if the intra-membrane and bulk gas
165 phase fractions exhibit different T_2 values, as was the case for the samples loaded with CH_4 . For
166 this gas, the ^{13}C T_2 NMR measurements yielded two molecular ensembles with different T_2 NMR
167 relaxation times and the corresponding fractions (Table S7). These molecular ensembles were
168 attributed to the molecules inside the film and molecules in the bulk gas phase between the film
169 pieces (cf., Table S7). Multiplying the fraction related to the intra-membrane component with the
170 total mass of the gas obtained by NMR for the sample region containing the MMM provided an
171 estimation of the intra-membrane concentration. This approach yielded the same intra-membrane
172 concentration for methane, within uncertainty, as that based on the mass balance (Tables S4 and
173 S6). The method based on the ^{13}C T_2 NMR measurements could not be used for CO_2 because for
174 this gas only a single T_2 NMR relaxation time was measured in the studied MMM samples.

175

176 **2.5 PFG NMR measurements**

177 NMR measurements were performed mainly using a 14 T Avance III spectrometer and selected
178 measurements were performed using a 17.6 T Avance III HD spectrometer (Bruker Biospin)
179 operating at ^{13}C frequencies of 149.8 MHz and 188.6 MHz, respectively. The magnetic field
180 gradients with amplitudes up to 23 T/m were generated using a *Diff30* diffusion probe at 14 T and
181 a *Diff50* diffusion probe at 17.6 T. Selected experiments were also performed using a *DiffBB*
182 diffusion probe at 14 T to ensure the reliability and consistency of the data. The relatively high
183 maximum magnetic field gradient strength allowed diffusion to be quantified for molecular
184 displacement as small as 0.5 μm , which was recorded for gas molecules diffusing mostly in the
185 polymer phase of MMMs. No significant differences were observed between the data measured
186 using the two spectrometers and the different diffusion probes, confirming the absence of any
187 measurement artifacts. Bipolar, sine and trapezoidal shaped magnetic field gradient pulses were
188 used with effective pulse durations between 1.4 ms and 3 ms. The total time needed to perform a
189 PFG NMR measurement to obtain a single self-diffusivity value ranged between 1 and 6 h with a
190 total number of scans between 144 and 512, depending on the signal to noise ratio. The repetition
191 delays used were between 3 and 6 s, which is at least 1.5 times greater than the T_1 relaxation time.
192 The diffusion time ranged from 7 ms to 1.28 s for both CO_2 and CH_4 diffusion. ^{13}C PFG NMR
193 was used rather than the more common ^1H PFG NMR to take advantage of the longer T_2 relaxation
194 time of the ^{13}C nuclei of guest molecules in MMMs. The ^{13}C NMR spectrum for CO_2 and CH_4
195 consisted of a single non-overlapping line with chemical shifts of around 150 and 4 ppm,
196 respectively.

197 The diffusion experiments were conducted using the 13-interval pulse sequence [26] using
198 bipolar gradients that were modified with the addition of a longitudinal eddy current delay[27].
199 This sequence was used to minimize or eliminate inhomogeneities in the magnetic field (*i.e.*,
200 magnetic susceptibility effects). Such inhomogeneities are expected for heterogeneous systems
201 such as stacked film pieces that were used in this work. Each self-diffusivity was obtained from
202 the dependence of the normalized PFG NMR signal on the amplitude of the magnetic field gradient
203 (g). This dependence is known as a PFG NMR attenuation curve, which, in the case of normal
204 diffusion when all studied molecules diffuse with the same self-diffusion coefficient, can be
205 described by the following equation [28]:

$$206 \quad \psi = \frac{S(g)}{S(g \sim 0)} = \exp(-q^2Dt), \quad (1)$$

207
208 where ψ is the PFG NMR signal attenuation, S is the PFG NMR signal at gradient strength g , t is
209 the diffusion time (*i.e.*, the diffusion observation time) [26] and $q = 2\gamma\delta g$, where γ , is the
210 gyromagnetic ratio, and δ is the effective duration of one gradient pulse. In the case of three-
211 dimensional diffusion, the root mean square displacement (RMSD) can be related to the self-
212 diffusivity by using the Einstein relation [28]:

$$213 \quad \langle r^2 \rangle^{1/2} = \sqrt{6Dt}, \quad (2)$$

214
215
216 In the case of two molecular ensembles diffusing with different self-diffusivities the attenuation
217 equation can be written as follows:

$$218 \quad \psi = \frac{S(g)}{S(g \sim 0)} = \sum_{i=1}^n p_i \exp(-D_i q^2 t), \quad (3)$$

219
220 where p_i and D_i are, respectively, the population fraction and the self-diffusivity of ensemble i .
221 The self-diffusivities and the fractions were calculated by fitting and using least-squares regression
222 to Eq. 3 on the measured PFG NMR attenuation curves with the constraint that $\sum p_i = 1$. The
223 experimental error was determined by considering the following: (i) the reproducibility of data
224 when measurements of the same sample were performed using the different spectrometers (14 T
225 and 17.6 T) under the same experimental conditions and (ii) the reproducibility of data from
226 measurements under the same experimental conditions of two identically prepared (but different)
227 samples. The total experimental uncertainty was around 25% under most experimental conditions.

228
229 Longitudinal (T_1) and transverse (T_2) ^{13}C NMR relaxation times of the sorbates were
230 determined using the standard inversion recovery and standard Carr-Purcell-Meiboom-Gill
231 (CPMG) pulse sequences, respectively. The tau value used in the CPMG experiments was 100 μs .
232 T_1 measurements showed the presence of 2 ensembles with different T_1 times; one ensemble was
233 attributed to molecules mostly diffusing inside the membrane film and the second to the molecules
234 mostly diffusing in the gas phase outside the membrane film (Table S7). It is important to note that
235 due to relatively large T_1 measurement times there is a significant exchange between the film and
236 gas phase environments. The ensemble assignment was based on the comparison with the
237 corresponding relaxation data obtained for the pure bulk gas phase (no membrane film added).
238 The two ensembles were observed for both methane and carbon dioxide under our T_1 measurement
239 conditions. Table S7 shows the T_1 results obtained for different samples studied. In the case of T_2
240 NMR relaxation measurements, two molecular ensembles with different T_2 times were observed
241 only for methane. These ensembles were attributed to gas molecules located inside and outside the

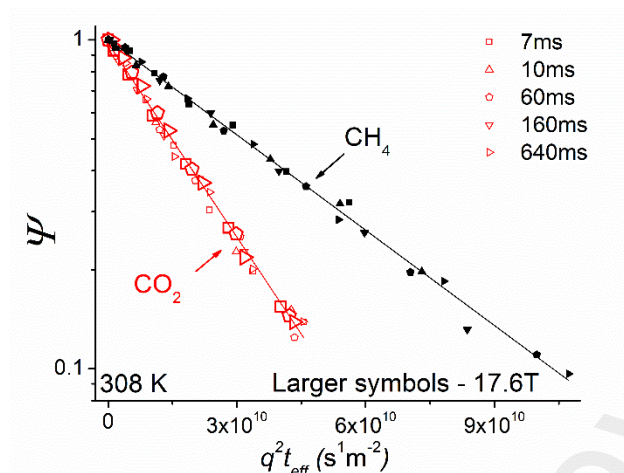
242 film. Biexponential fitting was used to quantify the fractions and their corresponding T_2 relaxation
243 times for the MMM samples. The ensembles were assigned in the same way as identified above
244 for T_1 . The relaxation measurements were also conducted for pure 6FDA-Durene loaded with
245 single-component gases (Table S8). All NMR relaxation data are presented in Tables S7 and S8.

246

247 **3. Results and Discussion**

248 Diffusion measurements were first performed for the MMM with 12.5 wt% loading of
249 UiO-66-NH₂, which corresponds to approximately 14 vol%. In this membrane significant space
250 between neighboring MOF crystals is expected on average. Thus, these experiments are useful in
251 evaluating if particles are well dispersed, which will result in mono-exponential behavior in the
252 attenuation curves.

253 Fig. 1 shows examples of the ¹³C PFG NMR attenuation curves measured for CO₂ and CH₄
254 diffusing in a 12.5 wt% UiO-66-NH₂/6FDA-Durene MMM for diffusion times in the range
255 between 7 and 640 ms at 308 K. Additional examples of ¹³C PFG NMR for measurements
256 performed with these samples at a lower temperature of 253 K are presented in the Supplementary
257 Materials section (Fig. S4). While these experiments and most of the experiments to be presented
258 later were conducted at 14 T, some additional complementary experiments were performed at a
259 higher magnetic field of 17.6 T to confirm that no measurement artifacts were present.



260

261 **Figure 1:** ^{13}C PFG NMR attenuation curves measured in a 12.5 wt% UiO-66-NH₂/6FDA-
 262 Durene MMM loaded with CO₂ (empty symbols) and CH₄ (filled symbols) at 308 K. All
 263 measurements were performed at 14 T unless indicated otherwise in the figure.

264

265 The observed coincidence of the data, within uncertainty, confirms the reproducibility and
 266 reliability of the measured results (see examples in Fig. 1). It can be seen in Figs. 1 and S4 that the
 267 attenuation curves for both CO₂ and CH₄ exhibit a mono-exponential behavior (i.e., linear in the
 268 semi-logarithmic representation of the figures) and no dependence on diffusion time. This
 269 observed behavior agrees well with Eq. 1, as can be observed by the average fitted lines to this
 270 equation in the figures. These lines correspond to single self-diffusivities independent of the
 271 diffusion time for each sorbate, sample, and temperature. Based on these data it can be concluded
 272 that the membrane transport properties remain uniform within the studied range of diffusion times
 273 (7 – 640 ms) and within the corresponding values of RMSDs (0.5 – 13 μm), which indicates
 274 uniform distribution of UiO-66-NH₂ crystals and no substantial interfacial defects. The values of
 275 RMSDs were calculated using Eq. 2 and are shown in Table S9. The lowest measured RMSD was
 276 comparable with the average crystal size (0.76 μm). Nevertheless, the self-diffusivity measured

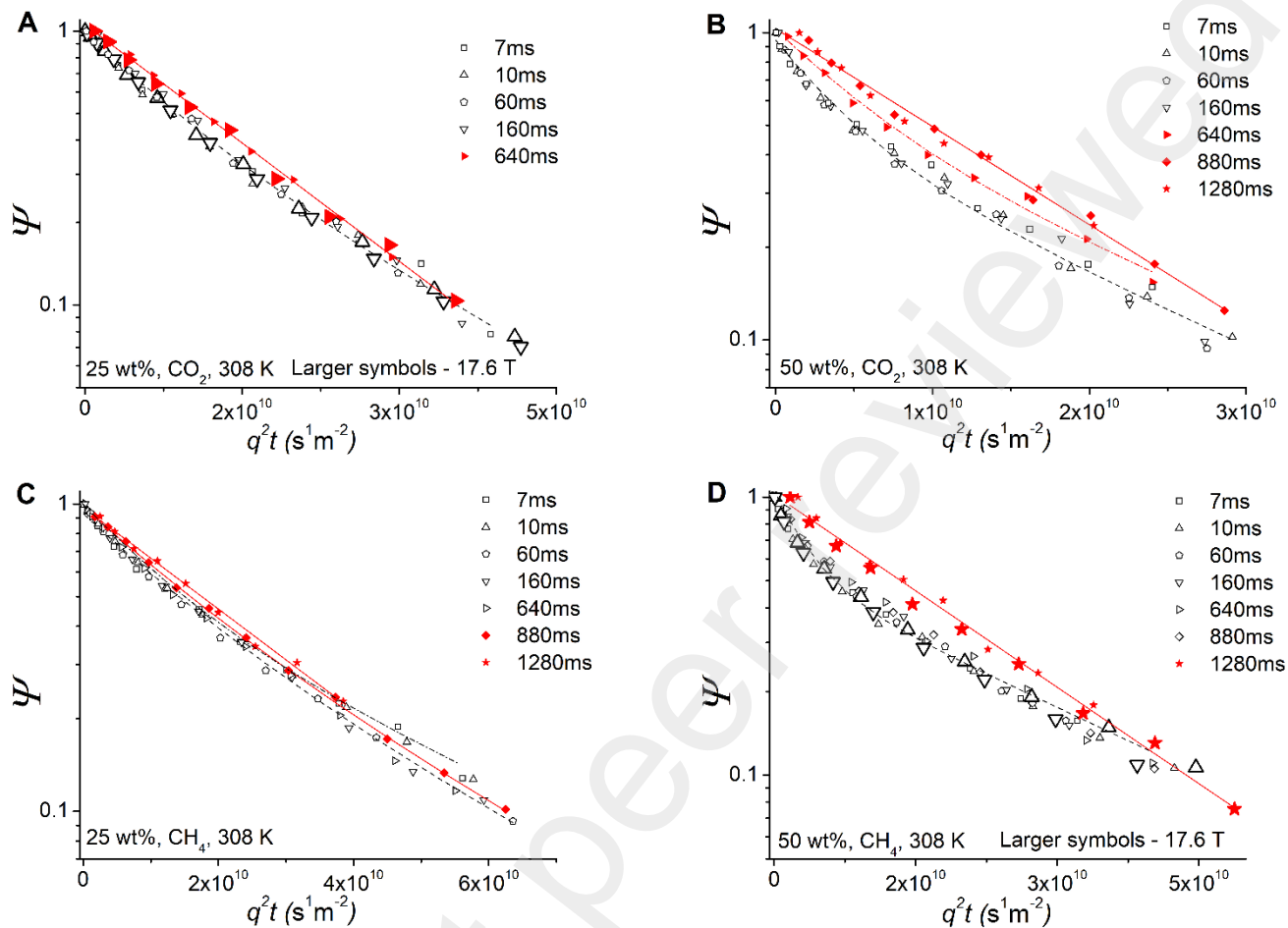
277 for both sorbates were attributed to molecules diffusing under conditions of fast exchange between
278 the UiO-66-NH₂ crystals and the polymer matrix under our measurement conditions.

279 These MMM results were compared to self-diffusivities of pure 6FDA-Durene at similar
280 sorbate loading pressures (Fig. S5 and Table S10). As anticipated, the MMMs have higher self-
281 diffusivities than the corresponding self-diffusivities in the pure polymer, a difference which can
282 be attributed to molecular exchange between MOF crystals and the polymer in the MMMs where
283 the intra-MOF diffusivity is expected to exceed that of intra-polymer diffusivity [10, 24].

284 In terms of transport performance, the largest benefits for MMMs occur at high MOF
285 loadings [3]. However, it is exceedingly difficult to capture *in situ* data on diffusion within discrete
286 phases of these composites [24, 29]. Given this limitation, most reports in the literature infer the
287 transport properties of MOF materials within an MMM by applying models, the most common of
288 which is the Maxwell model. Unfortunately, validating and improving these models is impossible
289 without directly accessing data on the underlying transport domains within these composite
290 materials. Our aim in this study is to extract quantifiable diffusion information within the polymer-
291 and MOF-rich domains of these MMMs, which provides direct *in situ* data on transport properties
292 within each phase. To accomplish this goal, we investigated higher MOF loadings, which should
293 result in larger quantities of MOF-rich domains, potentially enabling a deconvolution of diffusion
294 properties within the PFG NMR attenuation curves. In terms of MOF loading, our 25 wt% and 50
295 wt% samples correspond to loadings of 28 vol% and 54 vol%, respectively, so we are within the
296 loadings where clustering of the MOF phase can become significant. Previous studies by Vasenkov
297 *et al.* have used ¹³C PFG NMR to determine *in situ* transport properties for ZIF crystals inside
298 MMMs [10, 21, 25]. Polymer penetration into MOF materials has also been probed using similar
299 techniques, including work by Duan *et al.* [30], who used ¹³C NMR to probe the penetration of

300 poly(ethylene oxide) oligomers into UiO-66. However, to the best of our knowledge, no work has
301 previously been done to capture *in situ* data on the transport properties of UiO-66-NH₂ based
302 MMMs.

303 Figure 2 shows the ¹³C PFG NMR attenuation curves for CO₂ and CH₄ diffusing in the
304 MMMs with the higher MOF loadings of 25 wt% and 50 wt% for diffusion times in the range of
305 7 – 1280 ms at 308 K. As seen in Fig. 2, the coincidence of the data measured at 14 T and 17.6 T
306 indicates that our experiments are free of any magnetic susceptibility effects or any other
307 measurement artifacts. In contrast to the data obtained for the lower MOF loading (Fig. 1), the
308 PFG NMR attenuation curves in Fig. 2 show clear deviations from the mono-exponential behavior.
309 These deviations are more pronounced at short diffusion times and become much smaller at higher
310 diffusion times. In the limit of large diffusion times, mono-exponential behavior (*i.e.*, linear in the
311 presentation of Fig. 2) was observed. Such behavior indicates the presence of at least two
312 molecular ensembles diffusing with two different self-diffusivities at small diffusion times, while
313 fast molecular exchange between different membrane environments is approached in the limit of
314 large times. Analogous to our previous studies of MMMs [10, 21, 24] we used Eq. 3, which
315 assumes the existence of two molecular ensembles with different diffusivities, to fit the non-mono-
316 exponential attenuation curves in Fig. 2. The results of least square fitting using Eq. 3 can be seen
317 in Supplementary Materials section (Table S11).



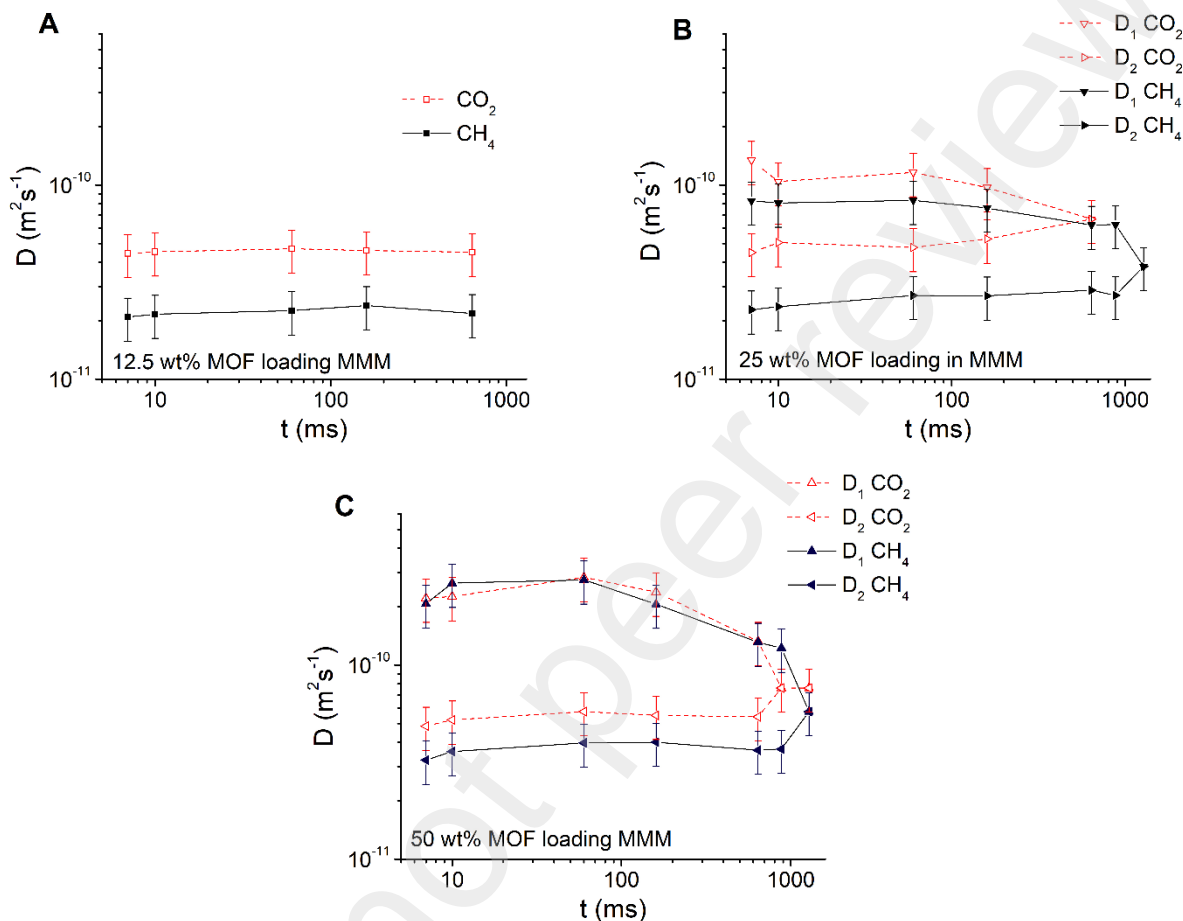
318
 319 **Figure 2:** ^{13}C PFG NMR attenuation curves measured in 25 wt% (A, C) and 50 wt% (B, D) UiO-
 320 66-NH₂/6FDA-Durene MMMs loaded with CO₂ (A, B) and CH₄ (C, D) performed at 14 T (unless
 321 indicated otherwise in the figure) using the 13-interval PFG NMR pulse sequence at 308 K. Solid
 322 symbols were used for attenuation curves consistent with the mono-exponential decay, within
 323 uncertainty. Solid lines represent the results of least-square fitting using Eq. 1. Dashed lines
 324 represent the results of least-square fitting using Eq. 3.

325 Under our measurement conditions, the PFG NMR signal from the gas molecules diffusing
 326 outside the membrane films is attenuated at the smallest gradient strength used, eliminating any
 327 bulk gas-phase influence on the measured signal. Therefore, the deviations from the mono-

328 exponential behavior can be explained only by the existence of different molecular ensembles
329 inside the MMMs. The two intra-membrane ensembles observed in the measurements were
330 attributed to molecules diffusing mostly inside MOFs and through MOF–polymer interphases
331 (ensemble 1 with a faster diffusivity, D_1), and to molecules mostly diffusing inside the polymer
332 phase (ensemble 2 with a slower diffusivity, D_2). This assignment was confirmed by the
333 observation that the diffusivities of intra-polymer ensemble 2 were approaching the corresponding
334 diffusivities measured in a pure 6FDA-Durene polymer (compare data presented in Tables S10
335 and S11). The PFG NMR observation of ensemble 1 under the conditions when RMSDs
336 significantly exceed the size of a single MOF crystal provides evidence for the formation of MOF
337 clusters, which can be expected at higher MOF loadings that were used. The self-diffusion data
338 measured at a lower temperature of 253 K similarly showed the trend of a transition from a bi-
339 exponential behavior to that approaching mono-exponential at longer diffusion times, thus
340 confirming our conclusion about the existence of the two ensembles of gas molecules related to
341 MOF clustering in the MMMs (Fig. S6).

342 The dependence of the measured self-diffusivities on the diffusion time of CO₂ and CH₄ in
343 the different MOF loading MMMs at 308 K is presented in Fig. 3. The corresponding plots for 253
344 K can be seen in Fig. S7. Fig. 3A shows a single self-diffusivity for each gas plotted as a function
345 of diffusion time for a 12.5 wt% UiO-66-NH₂/6FDA-Durene MMM. In this case there is no or
346 little MOF crystal clustering, and the condition of fast exchange of the molecules diffusing
347 between the MOF and polymer phase is fulfilled for each measured diffusion time. Clearly, in this
348 case there is also no dependence on RMSD (Figs. S8A and S9A). This result also provides
349 evidence of uniform transport properties of the UiO-66-NH₂/6FDA-Durene membrane for the

350 range of the RMSD values used. Figs. 3B and 3C show the dependence of the self-diffusivities of
351 the ensembles 1 and 2 discussed above on diffusion time.



352 **Figure 3:** CO_2 (empty symbols) and CH_4 (filled symbols) self-diffusivities plotted as a function
353 of diffusion time in UiO-66-NH₂/6FDA-Durene MMM samples with MOF loadings of 12.5 wt%
354 (A), 25 wt% (B), and 50 wt% (C) at 308 K. D_1 and D_2 represent the self-diffusivities of
355 ensembles 1 and 2, respectively, discussed in the text.

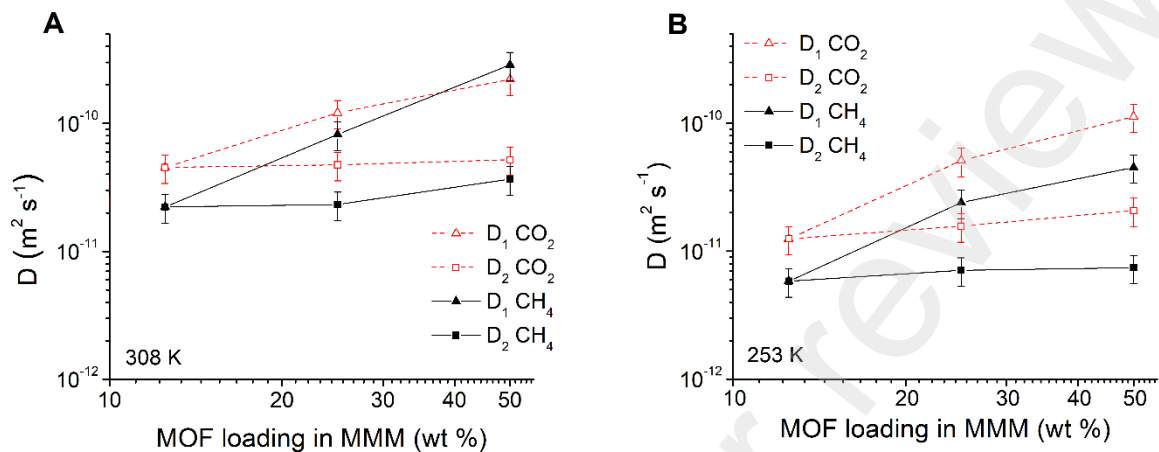
356
357 In the limit of large diffusion times the diffusivities of both ensembles approach the same value
358 corresponding to a fast exchange between different membrane environments. The data in these

359 figures can be used to estimate the sizes of MOF clusters in the MMMs with 25 wt% and 50 wt%
360 MOF loadings. This size is expected to be approximately equal to the RMSD at the point of
361 convergence where two diffusivities merge into a single value. In the case of the MMM loaded
362 with 25 wt% MOF, the estimated cluster size for CO₂ was approximately $16 \pm 2 \mu\text{m}$, and around
363 $17 \pm 2 \mu\text{m}$ for CH₄. These values are the same, within uncertainty, which support the interpretation
364 of our data because the MOF cluster size should not depend on the sorbate type. For the 50 wt%
365 MMM, larger cluster sizes were estimated, approximately $20 \pm 2 \mu\text{m}$ for CO₂ and around 21 ± 2
366 μm for CH₄. Some increase in the cluster size for the 50 wt% MMM is expected due to a higher
367 concentration of UiO-66-NH₂ crystals in this sample. It is important to note that the cluster sizes
368 were estimated based only on the data for 308 K. The maximum measured RMSDs were somewhat
369 smaller at a lower temperature of 253 K, which precluded the evaluation at conditions where D_1
370 and D_2 are the same.

371 Under our experimental conditions, the CO₂ self-diffusivity in all three studied MMMs
372 shows a tendency to be higher than the corresponding self-diffusivity of CH₄ when compared for
373 the same molecular ensemble, MMM sample, and temperature. This tendency is more pronounced
374 for the intra-polymer ensemble (ensemble 2) than for the intra-MOF ensemble (ensemble 1). The
375 observed diffusivity difference can be understood based on the smaller size of CO₂ (3.3 Å)
376 molecules in comparison to CH₄ molecules (3.8 Å) [31].

377 Fig. 4 shows self-diffusivities plotted as a function of the MOF loadings in the MMMs for
378 two different temperatures (308 and 253 K) at a diffusion time of 10 ms, which represents the
379 smallest diffusion time limit common for all studied samples. This diffusion time was selected to
380 minimize the influence of a molecular exchange between different MMM environments on the

381 measured diffusivities. It is seen that the faster self-diffusivity (D_1) increases with increasing MOF
382 loading.



383
384 **Figure 4:** Self-diffusivities of CO_2 (empty symbols) and CH_4 (filled symbols) in the limit of
385 small diffusion time (10 ms) plotted as a function of MOF loading in the MMM for 308 K (A)
386 and 253 K (B)

387
388 This finding can be attributed to a larger extent of MOF crystal clustering and/or formation of
389 some free volume defects at the interfaces between MOF crystals as the MOF loading increases.
390 At the same time, the slower diffusivity (D_2) which is related to molecules diffusing mostly in the
391 polymer phase remains the same, within uncertainty. The latter diffusivity is similar to that in the
392 pure polymer film without MOF (Fig. S10). In gas separations, diffusion selectivity can be defined
393 as the ratio of intra-membrane diffusivities for the studied pair of sorbates. This information can
394 be gleaned from Fig. 4, which shows that the average diffusion selectivity for ensemble 1 (intra-
395 MOF diffusion) is only around 2. As the MOF loading increases, the diffusion selectivity for this
396 ensemble stays roughly the same or even decreases. This result is not surprising when considering

397 the sizes of CO₂ and CH₄ (3.3 and 3.8 Å, respectively), which are significantly smaller than the
398 UiO-66-NH₂ pore aperture size (around 6 Å) [32] so no large size-sieving effects are expected.
399 The small diffusion selectivity observed for ensemble 1 (intra-MOF diffusion) is also consistent
400 with an occurrence of some free volume defects at the interfaces between neighboring MOF
401 crystals. The gas diffusivity values and diffusion selectivity for ensemble 2 (intra-polymer
402 diffusion) remains constant, irrespective of an increase in the MOF loading (Fig. 4). The latter
403 result indicates that the polymer properties governing diffusion of the studied gases in the polymer
404 phase remain mostly unchanged as the MOF loading increases. It is important to note that the
405 MMM type selected for this work is promising for CH₄/CO₂ separations mostly due to a
406 remarkable sorption selectivity [9, 18], which is not studied in this work.

407 To ensure the validity of the presented comparison between the CH₄ and CO₂ self-
408 diffusivities, which were measured at slightly different intra-MOF and intra-MMM loadings,
409 complementary PFG NMR measurements were conducted at several different gas intra-membrane
410 concentrations. These studies confirmed that minor deviations in the gas concentrations do not
411 significantly affect the results of the analysis of the diffusivities across different samples. The data
412 presented in Figs. S10, S11 reveal a lack of any significant gas concentration dependence of the
413 measured self-diffusivities.

414 The activation energy of diffusion was estimated by analyzing the self-diffusivity data at
415 two different temperatures. While the experimental uncertainty is relatively large, Table S12
416 shows that there is no significant dependence of the activation energy of diffusion on the MOF
417 loading for any particular gas type and molecular ensemble (intra-MOF or intra-polymer).
418 However, the activation energy data show a tendency of a higher activation energy for CH₄ than

419 for CO₂ for intra-MOF ensemble. This observation can be attributed to a larger molecular size of
420 the former gas.

421 The performance of MOF-based MMMs depends significantly on MOF composition and MOF
422 loading, but there are few studies that quantify MOF clustering effects, and – to the best of our
423 knowledge – none that reported direct measurements of diffusion inside MOF clusters for UiO
424 subclass of MOFs or any other MOF type. In this study, our findings reveal the formation of two
425 phases: a MOF-rich phase with effective domain sizes large enough to be observed within the
426 resolution of PFG NMR and a polymer phase. Interestingly, the features for the MOF-rich phase
427 become apparent for MOF loadings ≥ 25 wt% (≥ 28 vol%), and the theoretical percolation
428 threshold (0.31 for site percolation of randomly packed hard spheres) is expected to occur in the
429 same range of MOF loadings, assuming the MOF particles are approximated as spheres [33].
430 However, formation of the spanning MOF cluster, viz a cluster of interconnected MOF crystals
431 spanning an entire MMM as well as a related step change in diffusivity, which would be expected
432 as MOF loadings surpassed the percolation limit, were not observed for either CO₂ or CH₄. This
433 finding suggests a mechanism of physical priming during the preparation of casting solutions
434 followed by cluster formation. Physical priming is the phenomenon of polymer adsorption onto
435 MOFs to form a soft polymer shell when suspensions are prepared [34]. Thus, there is some mass
436 transfer resistance from the polymer at the MOF interface that precludes significant MOF–MOF
437 contact, but at high enough MOF loadings, particles will begin to form networks of clusters. These
438 findings are common in other MMM formed with 6FDA-based polyimides. Notably, Zhang *et al.*
439 studied MMMs formed from ZIF-8 and 6FDA-DAM with loadings up to 48 wt% for
440 propylene/propane separations and observed continuous increases in permeability and selectivity

441 without a step change in permeability that would be characteristic of diffusion effects at percolation
442 [35].

443 A clear path to substantial improvements in the separation performance of MOF-based
444 MMMs can be related to increasing MOF loadings to an extent where diffusion pathways through
445 an entire membrane become available only via MOF crystals and thin interfaces between the
446 neighboring crystals. The availability of such pathways corresponds to the percolation over the
447 MOF phase in MMMs, i.e., the existence of a spanning cluster of interconnected MOF crystals
448 discussed above. In this work, we quantified for the first time the average sizes of clusters of
449 interconnected MOF crystals and the intra-cluster diffusivity using microscopic diffusion
450 measurements. It was observed that with increasing MOF loading there is a tendency for an
451 increase of both the cluster sizes and intra-cluster diffusivity. The reported quantification of the
452 MOF cluster growth as a function of MOF loading is required for a better understanding of the
453 process of reaching conditions of percolation over the MOF phase in MMMs. Larger increases in
454 the MOF loading leading to larger MOF clusters can require functionalization of the external MOF
455 crystal surface to avoid occurrence of intra-membrane defects and form mechanically stable
456 MMMs. This approach will be explored in our future research.

457

458 **4. Conclusion**

459 ¹³C PFG NMR was applied to study the self-diffusion of CO₂ and CH₄ in UiO-66-
460 NH₂/6FDA-Durene mixed matrix membranes as a function of increasing MOF loading. The
461 PFG NMR measurements were performed for a broad range of diffusion times and the
462 corresponding RMSDs, which were comparable to or larger than the average UiO-66-NH₂

463 crystal size. These diffusion studies demonstrated that as the MOF loading in the MMM is
464 increased beyond 12.5 wt% of MOF, two molecular ensembles with different diffusivities and
465 fractions are observed for both gases considered in this study: i) an ensemble corresponding to
466 diffusion inside clusters of MOF crystals, and ii) an ensemble corresponding to diffusion
467 mostly inside the polymer phase of the membrane samples. Quantification of the MOF cluster
468 sizes revealed a direct correlation with the intra-membrane MOF loading. As the MOF loading
469 increased, so did the cluster sizes. Furthermore, gas self-diffusivity inside clusters of MOF
470 crystals showed a tendency to become larger with increasing MOF loading. The latter increase
471 can be related to a tighter packing of MOF crystals inside the clusters and creation of some
472 free volume defects at the interfaces between the neighboring MOF crystals with an increase
473 in the MOF loading. Functionalization of the external surface MOF crystals to improve the
474 properties of the interfaces in such clusters will be explored in our future research.

475

476 **Acknowledgements**

477 The present work was financially supported by NSF (CBET award No. 2034734 and
478 2034742). A portion of this work was performed in the McKnight Brain Institute at the National
479 High Magnetic Field Laboratory's Advanced Magnetic Resonance Imaging and Spectroscopy
480 (AMRIS) Facility, which is supported by National Science Foundation Cooperative Agreement
481 DMR-1644779, DMR-2128556 and the State of Florida. This work was supported in part by an
482 NIH award, S10 RR031637, for magnetic resonance instrumentation.

483

484

485 **References**

- 486 [1] D.S. Sholl, R.P. Lively, Seven chemical separations to change the world, *Nature* 532 (2016)
487 435-437. <https://doi.org/10.1038/532435a>.
- 488 [2] R.W. Baker, K. Lokhandwala, Natural Gas Processing with Membranes: An Overview, *Ind.*
489 *Eng. Chem. Res.* 47 (2008) 2109-2121. <https://doi.org/10.1021/ie071083w>.
- 490 [3] M. Galizia, W.S. Chi, Z.P. Smith, T.C. Merkel, R.W. Baker, B.D. Freeman, 50th Anniversary
491 Perspective: Polymers and Mixed Matrix Membranes for Gas and Vapor Separation: A Review
492 and Prospective Opportunities, *Macromolecules* 50 (2017) 7809-7843.
493 <https://doi.org/10.1021/acs.macromol.7b01718>.
- 494 [4] Q. Qian, P.A. Asinger, M.J. Lee, G. Han, K. Mizrahi Rodriguez, S. Lin, F.M. Benedetti, A.X.
495 Wu, W.S. Chi, Z.P. Smith, MOF-Based Membranes for Gas Separations, *Chem. Rev.* 120 (2020)
496 8161-8266. <https://doi.org/10.1021/acs.chemrev.0c00119>.
- 497 [5] Y. Jiang, C. Liu, J. Caro, A. Huang, A new UiO-66-NH₂ based mixed-matrix membranes
498 with high CO₂/CH₄ separation performance, *Microporous Mesoporous Mater.* 274 (2019) 203-
499 211. <https://doi.org/https://doi.org/10.1016/j.micromeso.2018.08.003>.
- 500 [6] L.M. Robeson, Correlation of separation factor versus permeability for polymeric
501 membranes, *J. Membr. Sci.* 62 (1991) 165-185. [https://doi.org/https://doi.org/10.1016/0376-
502 7388\(91\)80060-J](https://doi.org/https://doi.org/10.1016/0376-7388(91)80060-J).
- 503 [7] L.M. Robeson, The upper bound revisited, *J. Membr. Sci.* 320 (2008) 390-400.
504 <https://doi.org/https://doi.org/10.1016/j.memsci.2008.04.030>.
- 505 [8] K. Chen, K. Xu, L. Xiang, X. Dong, Y. Han, C. Wang, L.-B. Sun, Y. Pan, Enhanced
506 CO₂/CH₄ separation performance of mixed-matrix membranes through dispersion of sorption-

507 selective MOF nanocrystals, *J. Membr. Sci.* 563 (2018) 360-370.
508 <https://doi.org/https://doi.org/10.1016/j.memsci.2018.06.007>.

509 [9] Q. Qian, A.X. Wu, W.S. Chi, P.A. Asinger, S. Lin, A. Hypsher, Z.P. Smith, Mixed-Matrix
510 Membranes Formed from Imide-Functionalized UiO-66-NH₂ for Improved Interfacial
511 Compatibility, *ACS Appl. Mater. Interfaces.* 11 (2019) 31257-31269.
512 <https://doi.org/10.1021/acsami.9b07500>.

513 [10] R. Mueller, V. Hariharan, C. Zhang, R. Lively, S. Vasenkov, Relationship between mixed
514 and pure gas self-diffusion for ethane and ethene in ZIF-8/6FDA-DAM mixed-matrix membrane
515 by pulsed field gradient NMR, *J. Membr. Sci.* 499 (2016) 12-19.
516 <https://doi.org/https://doi.org/10.1016/j.memsci.2015.10.036>.

517 [11] H. Daglar, S. Aydin, S. Keskin, MOF-based MMMs breaking the upper bounds of polymers
518 for a large variety of gas separations, *Separ. Purif. Technol.* 281 (2022) 119811.
519 <https://doi.org/https://doi.org/10.1016/j.seppur.2021.119811>.

520 [12] E.M. Forman, A. Baniani, L. Fan, K.J. Ziegler, E. Zhou, F. Zhang, R.P. Lively, S.
521 Vasenkov, Ethylene diffusion in crystals of zeolitic imidazole Framework-11 embedded in
522 polymers to form mixed-matrix membranes, *Microporous Mesoporous Mater.* 274 (2019) 163-
523 170. <https://doi.org/https://doi.org/10.1016/j.micromeso.2018.07.044>.

524 [13] V. Muthukumaraswamy Rangaraj, M.A. Wahab, K.S.K. Reddy, G. Kakosimos, O. Abdalla,
525 E.P. Favvas, D. Reinalda, F. Geuzebroek, A. Abdala, G.N. Karanikolos, Metal Organic
526 Framework — Based Mixed Matrix Membranes for Carbon Dioxide Separation: Recent
527 Advances and Future Directions, *Front. Chem.* 8 (2020).
528 <https://doi.org/10.3389/fchem.2020.00534>.

529 [14] W. Chai, Y. Shen, J. Wang, G. Zhang, Applications of Metal-Organic Framework Materials,
530 J. Phys. Conf. Ser. 2194 (2022) 012014. <https://doi.org/10.1088/1742-6596/2194/1/012014>.

531 [15] J. Winarta, B. Shan, S.M. McIntyre, L. Ye, C. Wang, J. Liu, B. Mu, A Decade of UiO-66
532 Research: A Historic Review of Dynamic Structure, Synthesis Mechanisms, and
533 Characterization Techniques of an Archetypal Metal–Organic Framework, Cryst. Growth Des.
534 20 (2020) 1347-1362. <https://doi.org/10.1021/acs.cgd.9b00955>.

535 [16] J.H. Cavka, S. Jakobsen, U. Olsbye, N. Guillou, C. Lamberti, S. Bordiga, K.P. Lillerud, A
536 New Zirconium Inorganic Building Brick Forming Metal Organic Frameworks with Exceptional
537 Stability, J. Am. Chem. Soc. 130 (2008) 13850-13851. <https://doi.org/10.1021/ja8057953>.

538 [17] M. Kandiah, M.H. Nilsen, S. Usseglio, S. Jakobsen, U. Olsbye, M. Tilset, C. Larabi, E.A.
539 Quadrelli, F. Bonino, K.P. Lillerud, Synthesis and Stability of Tagged UiO-66 Zr-MOFs, Chem.
540 Mater. 22 (2010) 6632-6640. <https://doi.org/10.1021/cm102601v>.

541 [18] M.Z. Ahmad, M. Navarro, M. Lhotka, B. Zornoza, C. Téllez, W.M. de Vos, N.E. Benes,
542 N.M. Konnertz, T. Visser, R. Semino, G. Maurin, V. Fila, J. Coronas, Enhanced gas separation
543 performance of 6FDA-DAM based mixed matrix membranes by incorporating MOF UiO-66 and
544 its derivatives, J. Membr. Sci. 558 (2018) 64-77.
545 <https://doi.org/https://doi.org/10.1016/j.memsci.2018.04.040>.

546 [19] G.E. Cmarik, M. Kim, S.M. Cohen, K.S. Walton, Tuning the Adsorption Properties of UiO-
547 66 via Ligand Functionalization, Langmuir 28 (2012) 15606-15613.
548 <https://doi.org/10.1021/la3035352>.

549 [20] J. Winarta, A. Meshram, F. Zhu, R. Li, H. Jafar, K. Parmar, J. Liu, B. Mu, Metal–organic
550 framework-based mixed-matrix membranes for gas separation: An overview, J. Polym. Sci. 58
551 (2020) 2518-2546. <https://doi.org/https://doi.org/10.1002/pol.20200122>.

552 [21] R. Mueller, S. Zhang, C. Zhang, R. Lively, S. Vasenkov, Relationship between long-range
553 diffusion and diffusion in the ZIF-8 and polymer phases of a mixed-matrix membrane by high
554 field NMR diffusometry, *J. Membr. Sci.* 477 (2015) 123-130.
555 <https://doi.org/https://doi.org/10.1016/j.memsci.2014.12.015>.

556 [22] M. Dvoyashkin, J. Zang, G.I. Yucelen, A. Katihar, S. Nair, D.S. Sholl, C.R. Bowers, S.
557 Vasenkov, Diffusion of Tetrafluoromethane in Single-Walled Aluminosilicate Nanotubes:
558 Pulsed Field Gradient NMR and Molecular Dynamics Simulations, *J. Phys. Chem. C.* 116 (2012)
559 21350-21355. <https://doi.org/10.1021/jp3054247>.

560 [23] E.M. Forman, B.R. Pimentel, K.J. Ziegler, R.P. Lively, S. Vasenkov, Microscopic diffusion
561 of pure and mixed methane and carbon dioxide in ZIF-11 by high field diffusion NMR,
562 *Microporous Mesoporous Mater.* 248 (2017) 158-163.
563 <https://doi.org/https://doi.org/10.1016/j.micromeso.2017.04.041>.

564 [24] A. Baniani, M.P. Rivera, J. Marreiros, R.P. Lively, S. Vasenkov, Influence of polymer
565 modification on intra-MOF self-diffusion in MOF-based mixed matrix membranes, *Microporous*
566 *Mesoporous Mater.* 359 (2023) 112648.
567 <https://doi.org/https://doi.org/10.1016/j.micromeso.2023.112648>.

568 [25] A. Baniani, M.P. Rivera, R.P. Lively, S. Vasenkov, Quantifying diffusion of organic liquids
569 in a MOF component of MOF/Polymer mixed-matrix membranes by high field NMR, *J. Membr.*
570 *Sci.* 640 (2021) 119786. <https://doi.org/https://doi.org/10.1016/j.memsci.2021.119786>.

571 [26] R.M. Cotts, M.J.R. Hoch, T. Sun, J.T. Markert, Pulsed field gradient stimulated echo
572 methods for improved NMR diffusion measurements in heterogeneous systems, *J. Magn. Reson.*
573 83 (1989) 252-266. [https://doi.org/https://doi.org/10.1016/0022-2364\(89\)90189-3](https://doi.org/https://doi.org/10.1016/0022-2364(89)90189-3).

574 [27] S.J. Gibbs, C.S. Johnson, A PFG NMR experiment for accurate diffusion and flow studies
575 in the presence of eddy currents, *J. Magn. Reson.* 93 (1991) 395-402.
576 [https://doi.org/https://doi.org/10.1016/0022-2364\(91\)90014-K](https://doi.org/https://doi.org/10.1016/0022-2364(91)90014-K).

577 [28] J. Kärger, D.M. Ruthven, D.N. Theodorou, *Diffusion in Nanoporous Materials*, Wiley-
578 VCH, Weinheim, 2012.

579 [29] A. Baniani, S.J. Berens, M.P. Rivera, R.P. Lively, S. Vasenkov, Potentials and challenges of
580 high-field PFG NMR diffusion studies with sorbates in nanoporous media, *Adsorption* 27 (2021)
581 485-501. <https://doi.org/10.1007/s10450-020-00255-y>.

582 [30] P. Duan, J.C. Moreton, S.R. Tavares, R. Semino, G. Maurin, S.M. Cohen, K. Schmidt-Rohr,
583 Polymer Infiltration into Metal–Organic Frameworks in Mixed-Matrix Membranes Detected in
584 Situ by NMR, *J. Am. Chem. Soc.* 141 (2019) 7589-7595. <https://doi.org/10.1021/jacs.9b02789>.

585 [31] Y. Liu, G. Liu, C. Zhang, W. Qiu, S. Yi, V. Chernikova, Z. Chen, Y. Belmabkhout, O.
586 Shekhah, M. Eddaoudi, W. Koros, Enhanced CO₂/CH₄ Separation Performance of a Mixed
587 Matrix Membrane Based on Tailored MOF-Polymer Formulations, *Adv. Sci.* 5 (2018) 1800982.
588 <https://doi.org/https://doi.org/10.1002/advs.201800982>.

589 [32] F. Aghili, A.A. Ghoreyshi, A. Rahimpour, B. Van der Bruggen, New Chemistry for Mixed
590 Matrix Membranes: Growth of Continuous Multilayer UiO-66-NH₂ on UiO-66-NH₂-Based
591 Polyacrylonitrile for Highly Efficient Separations, *Ind. Eng. Chem. Res.* 59 (2020) 7825-7838.
592 <https://doi.org/10.1021/acs.iecr.9b07063>.

593 [33] C. Li, A. Qi, Y. Ling, Y. Tao, Y.-B. Zhang, T. Li, Establishing gas transport highways in
594 MOF-based mixed matrix membranes, *Sci. Adv.* 9 (2023) eadf5087.
595 <https://doi.org/doi:10.1126/sciadv.adf5087>.

596 [34] Q. Qian, P.A. Asinger, M.J. Lee, G. Han, K. Mizrahi Rodriguez, S. Lin, F.M. Benedetti,
597 A.X. Wu, W.S. Chi, Z.P. Smith, MOF-Based Membranes for Gas Separations, Chem. Rev. 120
598 (2020) 8161-8266. <https://doi.org/10.1021/acs.chemrev.0c00119>.

599 [35] C. Zhang, R.P. Lively, K. Zhang, J.R. Johnson, O. Karvan, W.J. Koros, Unexpected
600 Molecular Sieving Properties of Zeolitic Imidazolate Framework-8, J. Phys. Chem. Lett. 3
601 (2012) 2130-4. <https://doi.org/10.1021/jz300855a>.

602